ADVANCED FUNCTIONAL MATERIALS
www.afm-journal.de

Nitrogen-Doped Nanoporous Carbon/Graphene Nano-Sandwiches: Synthesis and Application for Efficient Oxygen Reduction

*Jing Wei, Yaoxin Hu, Yan Liang, Biao Kong, Jin Zhang, Jingchao Song, Qiaoliang Bao, George P. Simon, San Ping Jiang, and Huanting Wang**

A zeolitic-imidazolate-framework (ZIF) nanocrystal layer-protected carbonization route is developed to prepare N-doped nanoporous carbon/graphene nano-sandwiches. The ZIF/graphene oxide/ZIF sandwich-like structure with ultrasmall ZIF nanocrystals (i.e., ≈20 nm) fully covering the graphene oxide (GO) is prepared via a homogenous nucleation followed by a uniform deposition and confined growth process. The uniform coating of ZIF nanocrystals on the GO layer can effectively inhibit the agglomeration of GO during high-temperature treatment (800 °C). After carbonization and acid etching, N-doped nanoporous carbon/graphene nanosheets are formed, with a high specific surface area (1170 $m^2 g^{-1}$). These N-doped nanoporous carbon/graphene nanosheets are used as the nonprecious metal electrocatalysts for oxygen reduction and exhibit a high onset potential (0.92 V vs reversible hydrogen electrode; RHE) and a large limiting current density (5.2 mA cm^{-2} at 0.60 V). To further increase the oxygen reduction performance, nanoporous Co-N_x/carbon nanosheets are also prepared by using cobalt nitrate and zinc nitrate as cometal sources, which reveal higher onset potential (0.96 V) than both commercial Pt/C (0.94 V) and N-doped nanoporous carbon/graphene nanosheets. Such nanoporous Co-N_x/carbon nanosheets also exhibit good performance such as high activity, stability, and methanol tolerance in acidic media.

1. Introduction

Nanoporous carbon materials have received considerable attention because they exhibit a high specific surface area, large pore volume, high chemical and thermal stability, good conductivity, and high performance in the various applications involved adsorption, catalysis, as well as energy conversion and storage.[1] It should be noted that the incorporation of nitrogen atoms into the carbon lattice can significantly enhance the surface polarity, electric conductivity, and electron-donor tendency of the nanoporous carbons, resulting in an enhanced performance in the applications such as in fuel cells (i.e., oxygen reduction reaction, ORR), electric double-layer capacitors and batteries.[2] Recently, zeolitic imidazolate frameworks (ZIFs) have been demonstrated to be one of the attractive carbon precursors to prepare N-doped nanoporous carbon materials due to their highly microporous structure, regular morphology, and imidazole-based ligands with rich N atoms.[3–6] More importantly, the metal species (i.e., Zn, Co) from ZIFs also act as a hard template during the high-temperature carbonization, resulting in a highly porous structure after the removal of the corresponding metal nanoparticles. However, most of the ZIF-derived carbon materials show discrete nanoparticles, a highly porous structure, low graphitized degree and numerous defects; all of these would consequently lead to poor electrical conductivity and inevitably compromise the oxygen reduction activity required for fast electron transfer.[7]

Graphene, a 2D sp^2-hybridized carbon nanosheet, has been widely investigated as a candidate for electrochemical applications in fuel cells, batteries, and supercapacitors due to its excellent electrical properties and theoretically ultrahigh specific surface area (i.e., 2630 $m^2 g^{-1}$).[8] However, the graphene agglomerates easily because of the substantial loss of oxygen-containing groups during the reduction of graphene oxide (GO), resulting in a low specific surface area.[9] Consequently, the fast mass transportation required for a number of electrical processes such as ORR is inhibited. Different kinds of spacer materials were employed to prevent the agglomeration of graphene and increase the specific surface area of graphene.[10,11] An alternative route involves the incorporation of an ultrathin layer of nanoporous carbon, in particular nitrogen-doped nanoporous carbon, on the graphene surface, leading to the formation of

Dr. J. Wei, Y. X. Hu, Y. Liang, B. Kong, Prof. H. T. Wang
Department of Chemical Engineering
Monash University
Clayton, Victoria 3800, Australia
E-mail: huanting.wang@monash.edu
J. Zhang, Prof. S. P. Jiang
Fuels and Energy Technology Institute &
Department of Chemical Engineering
Curtin University
Perth, WA 6102, Australia
J. C. Song, Dr. Q. L. Bao, Prof. G. P. Simon
Department of Materials Engineering
Monash University
Clayton, Victoria 3800, Australia

DOI: 10.1002/adfm.201502311

a nanoporous carbon/graphene/nanoporous carbon sandwich-like structure with functionalization, high specific surface area and good electrical conductivity. The nanoporous carbon cannot only be employed as a spacer material to avoid the agglomeration of graphene, but can also be easily modified with other functional groups and metal (or metal oxide) nanoparticles which are included in the pores to broaden their applications.[4,12] Some reports have shown that the combination of nanoporous carbon thin layer on the graphene can enhance their performance in the electrochemical applications.[6,11,13] However, it remains challenging to coat a uniform, nanoporous thin carbon layer with heteroatom doping and metal species embedded on graphene, due to the weak interactions between the precursors of the functional carbon and graphene, as well as the severe agglomeration of graphene during the high-temperature treatment.

It is anticipated that coating a uniform ZIF-derived carbon thin layer on graphene to obtain the nanoporous carbon/graphene nanosheets with nitrogen-doping and (or) metal species loading is highly desirable in oxygen reduction reaction due to the combination of fast mass transport and electron transfer. To achieve this, a rational strategy is to prepare a uniform coating of ZIF nanoparticles on GO first and then convert the ZIF/GO nanosheets to designed nanoporous carbon/graphene nanosheets via high-temperature carbonization. Some reports have shown that ZIF-8 can be grown in situ on GO, as the strong interactions between the metal clusters from ZIF and oxygen-containing groups from GO.[6,14] However, most of examples show the resultant ZIF-8/GO composites have either random distributions of ZIF nanoparticles on the GO or the particle size of the ZIF is too large (>50 nm) due to the heterogeneous nucleation and very rapid growth rate of the ZIF. When using such ZIF-8/GO composites as precursors, the nanoporous carbon/graphene nanosheets with high specific surface area are difficult to obtain due to uncontrollable shrinkage and agglomeration of the graphene during the subsequent high-temperature treatment.

The deprotonation of imidazole from metal/imidazole complex is an important step during the nucleation of ZIF, which is usually hindered by GO due to its acidic groups (i.e., –COOH).[15] As a result, the existence of GO will inevitably affect the nucleation rate of ZIF located on its surface, leading to a heterogeneous nucleation process of ZIF on the GO surface and in the solution. To develop a simple route to control the growth process of ZIF on GO, is desirable to construct uniform ZIF/GO nanosheets with an ultrathin ZIF layer, as precursors to preparing N-doped, nanoporous carbon/graphene nanosheets with high specific surface area.

In this work we have demonstrated an ultrasmall ZIF nanocrystal layer protected carbonization method to N-doped nanoporous carbon/graphene nano-sandwiches. The ZIFs with diameter of around 20 nm are initially grown in a continuous fashion on both sides of graphene oxide to obtain ZIF/GO/ZIF sandwich-like structure. The strategy for this sandwich-like structure is via a homogenous nucleation, followed by uniform deposition and a confined growth process. After carbonization and acid etching, N-doped nanoporous carbon/graphene nano-sandwiches with high specific surface area (1170 m^2 g^{-1}) were readily obtained. The N-doped nanoporous carbon/graphene nanosheets are used as the non-precious metal electrocatalysts for the oxygen reduction in 0.1 M KOH, which reveal high onset potential (i.e., 0.92 V vs reversible hydrogen electrode; RHE), and large limiting current density (i.e., 5.2 mA cm^{-2} at 0.60 V). To further increase the oxygen reduction performance, nanoporous Co-N_x/carbon nanosheets are also prepared by using cobalt nitrate and zinc nitrate as cometal sources, which reveal higher onset potential (0.96 V) than both commercial Pt/C (0.94 V) and N-doped nanoporous carbon/graphene nanosheets. Furthermore, nanoporous Co-N_x/carbon nanosheets exhibit a good ORR activity in acidic media, with an onset potential (0.85 V) comparable to that of commercial Pt/C (0.93 V). Most importantly, they also reveal a higher stability and better methanol tolerance than Pt/C materials.

2. Results and Discussion

N-doped nanoporous carbon/graphene nanosandwiches were synthesized via deposition of ZIF nanocrystals on GO layer followed by carbonization and acid etching process, as illustrated in **Figure 1**. First, the zinc precursor was added to the imidazole solution to homogenously form the ZIF clusters (Figure 1, Step 1). Due to a strong coordination interaction between the metal ions from ZIF cluster and oxygen groups from GO, the cluster could be easily attached to both sides of GO. Second, the ZIF clusters on the GO layer grew further, resulting in

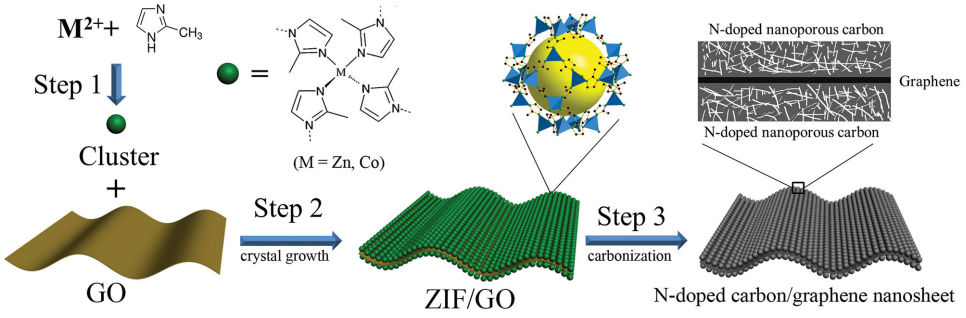

Figure 1. The schematic synthesis of N-doped nanoporous carbon/graphene nano-sandwiches. Step 1, homogeneous nucleation of zeolitic-imidazolate-frameworks (ZIFs) to form uniform clusters; Step 2, the deposition of ZIF clusters on the graphene oxide (GO) and confined growth of ZIF to form a ultrathin layer of ZIF on both sides of GO; Step 3, ZIF layer protected carbonization of ZIF/GO composited sheet and acid etching treatment to remove metal nanoparticles (i.e., Zn, Co).

an ultrathin ZIF layer fully covered GO nanosheet (Figure 1, Step 2). Finally, ZIF nanoparticles distributed on both sides of GO acted as a spacer and protective layer to prevent the severe agglomeration of reduced graphene oxide (rGO) during high-temperature treatment (Figure 1, Step 3). In addition, ZIF nanoparticles were converted to functional carbon materials with high specific surface area, nanoporous structure, and nitrogen-doping carbon framework. As a result, a new kind of N-doped nanoporous carbon/graphene sandwich-like structure was obtained.

ZIF-8, composed of Zn and imidazole, was the first material chosen to deposit on GO. After adding the Zn source to imidazole solution, the GO solution was immediately combined with the solution of ZIF. After stirring for 3 h, the products were collected by centrifugation and washing. The obtained ZIF-8/GO composites (denoted as Zn-ZIF/GO) were characterized using scanning electron microscopy (SEM) and transmission electron microscopy (TEM) technique. SEM image of Zn-ZIF/GO revealed the uniform nanosheet coated with ultrasmall ZIF-8 nanoparticles (**Figure 2**a). A high magnification SEM image showed ZIF nanoparticles aggregated together and nearly fully covering the GO surface (Figure 2b). To our knowledge, this is the first example of GO sheets fully covered by ZIF nanocrystals with ultrasmall diameter (<50 nm). Such a type of sandwich-like structure could effectively prevent the agglomeration of graphene during high-temperature treatment. Furthermore, GO fully covered by ZIF nanocrystals are very useful to the fabrication of catalysts for ORR, with a high density of active sites as ZIF is the catalyst precursor. TEM images further confirmed that the ZIF-8 nanoparticles with the diameter of around 20 nm were coated on GO uniformly (Figure 2c,d). Interestingly, some ZIF-8 crystals were located on the edge of GO and showed a well-defined crystal morphology, with larger crystal sizes than those located in the middle of GO sheet. This may be caused by the coming together of growth fronts of ZIF clusters located on the edge of both sides of GO. In addition, no ZIF nanoparticles are observed on the outside of the GO layer, indicating a strong binding of ZIF nanoparticles and GO. TEM images of ZIF/GO composites with different growth times (from 1 to 12 h) was also taken to investigate the deposition process of ZIF on GO (Figure S1, Supporting Information). The samples from 1 h growth showed that some areas of GO were not covered by ZIF nanoparticles due to the short deposition time. After 7 h, almost all the areas on GO were covered by ZIF nanoparticles, similar to the result of 3 h. After a longer time deposition (12 h), the particle size of ZIF on GO did not change obviously. Some additional large ZIF crystals (≈50 nm) were also observed, and located outside of GO. These crystals may be from the residual clusters in the solution, which further grow to form large crystals in the solution.

To investigate the possible growth mechanism of ZIF, the addition order of the precursors was changed. Zn salts in methanol were firstly added to the GO solution, followed by addition of imidazole solution. Using this in situ growth method, zinc ions were first adsorbed on GO sheets to act as a nucleation site. After addition of Zn precursor in GO solution, a slight agglomeration of GO in solution was observed. This is because the zinc ions act as a physical "crosslinker," GO tends to aggregate together to form 3D structure, like the GO hydrogel.[16] The imidazole solution was then added to in situ growth of ZIF on the GO sheets, with the resultant samples denoted as ZIF/GO-MIX. SEM image of ZIF/GO-MIX showed that the ZIF particles were not uniform (Figure S2, Supporting Information). Parts of ZIFs were located on GO, which revealed a small size. The others mixed with GO showed the crystal morphology of larger particle size. In addition, the ZIF/GO sheets also partly aggregated together to form 3D structures, due to the agglomeration of GO support induced by metal ions.

Comparison of these two different routes to mix the precursor showed that the order of addition of the precursor was an important aspect of the growth process of ZIF nanoparticles on the GO layer. In the first route, zinc ions were coordinated with imidazole to form metal/imidazole clusters via a deprotonation step. After the addition of the GO solution, the cluster readily attached to the GO layer due to a strong interaction between metal ions from cluster and the oxygen groups

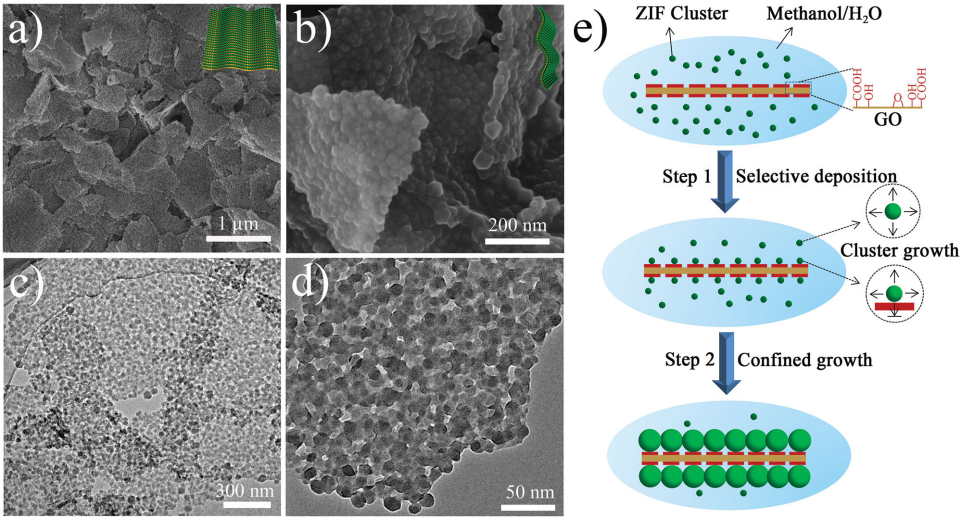

Figure 2. a,b) SEM images of Zn-ZIF/GO, the insets in (a) and (b) are corresponding diagrams of ZIF/GO structure viewed from different direction; c,d) TEM images of Zn-ZIF/GO composites; e) schematic of ZIF grown in the confined space to get ultrasmall ZIF nanocrystals fully covered on the GO.

from GO (Figure 2e). As the growth progressed, the clusters on GO layer turned to nanoparticles with a crystalline structure. Due to the limited space on the GO, the growth of particles was inhibited and thus the ZIF nanoparticles uniformly coated the GO. In the second synthetic route, as GO has insufficient numbers of oxygen groups to capture all the zinc ions, the metal ions were located either on GO or in the solution (Figure S2b, Supporting Information). Due to the acidic groups (such as –COOH) on the GO surface, the zinc ions on GO layer might show a slower deprotonation rate than that in the solution, leading to a heterogeneous nucleation. The clusters in the solution grew faster than those on the GO. Consequently, the obtained ZIF/GO composites showed the mixture of ZIF nanoparticles loaded on GO and discrete ZIF crystals.

As the uniform deposition of ZIF nanoparticles occurred on both sides of the GO, such sandwich-like structures should be able to prevent the agglomeration of GO effectively during high-temperature carbonization. The corresponding carbon materials were obtained by carbonization of Zn-ZIF/GO at 800 °C for 3 h followed by acid etching with 2 M HCl, which were denoted as Zn-ZIF/GO-800. SEM images of Zn-ZIF/GO-800 clearly revealed a carbon nanosheet structure (**Figure 3**a). Due to the severe shrinkage and crinkle of Zn-ZIF/GO during high-temperature carbonization, the derived carbon materials agglomerated partly. From the SEM image of the cross-section of carbon nanosheets, the carbon materials still revealed the well-reserved nanosheet morphology (Figure 3b). TEM images further confirmed this result (Figure 3c, Figure S3a,b, Supporting Information). The carbon nanosheets aggregated together to form a 3D structure. By comparing with TEM images of GO-800 prepared via carbonization of GO at 800 °C in Ar (Figure S4, Supporting Information), Zn-ZIF/GO-800 revealed a rough surface due to the coating of ZIF-derived carbon on graphene. The selective area electron diffraction (SAED) results of Zn-ZIF/GO-800 showed an amorphous carbon structure. By contrast, GO-800 revealed a polycrystalline graphite structure. The high magnification TEM images showed that a nanoporous carbon thin layer was coated uniformly on graphene sheet (Figure 3d, Figure S3c,d, Supporting Information), as seen by the less distinct wrinkles. In contrast to previous reports,[5] the ZIF crystal-derived carbon partially retained their crystalline morphology. In our results, when ultrasmall ZIF nanoparticles grew on GO, the ZIF-derived carbon did not show an obvious particle shape. This may be caused by a strong interaction of GO and ZIF. The GO can affect the carbonization process of ZIF. In addition, there was no zinc particles observed from TEM image, indicating the zinc particles were removed completely after the acid etching process. The nitrogen distributions were determined via scanning transmission electron microscopy (STEM) and element mapping technique shown in Figure S5, Supporting Information. The nitrogen atoms were distributed uniformly on the carbon nanosheet due to the unique sandwich-like structure. ZIF/GO-MIX was also carbonized under the same condition and the obtained carbon materials were denoted as ZIF/GO-MIX-800. TEM images of ZIF/GO-MIX-800 also revealed an aerogel-like structure. However, the carbon nanosheets were agglomerated more severely than that of Zn-ZIF/GO-800 (Figure S6, Supporting Information).

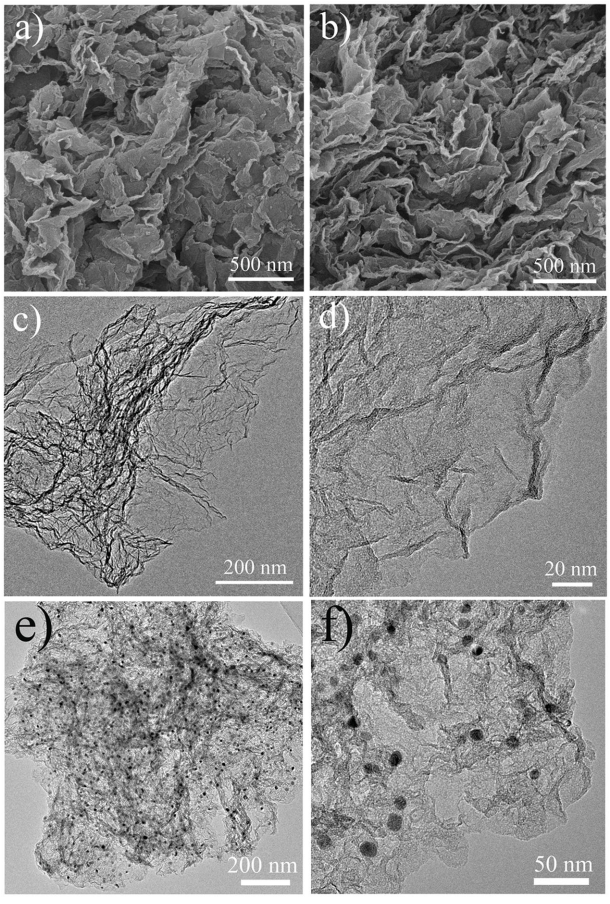

Figure 3. a,b) SEM images of N-doped nanoporous carbon/graphene nanosheets (Zn-ZIF/GO-800) with different orientations; c,d) TEM images of Zn-ZIF/GO-800 with different magnifications; e,f) TEM images of Co-Zn-ZIF/GO-800 by using zinc nitrate and cobalt nitrate as coprecursors.

In contrast to the zinc species in ZIF-8, the cobalt species in the ZIF play an important role in enhancing the ORR performance of the obtained carbon, as they can act as a catalyst to generate highly graphitized carbon and thus increase the electron transfer. Furthermore, cobalt species may also coordinate with N atoms in the carbon lattice such as pyridinic and pyrrolic nitrogen to form the Co-N_x-C clusters, which are more active than sole N-doped carbon for oxygen reduction catalysis.[17,18] In order to introduce Co species in the nanoporous carbon/graphene nanosheets, cobalt nitrate and zinc nitrate were used as cometal ion precursors and the obtained materials were denoted as Co-Zn-ZIF/GO. TEM image of Co-Zn-ZIF/GO revealed the ZIF nanoparticles were deposited on GO uniformly, similar to the Zn-ZIF/GO (Figure S7, Supporting Information). After carbonization under the same conditions (i.e., 800 °C in Ar) and acid etching, the resultant cobalt-containing carbon materials were denoted as Co-Zn-ZIF/GO-800. TEM image of Co-Zn-ZIF/GO-800 showed a 3D aerogel-like carbon materials with cobalt nanoparticles distributed uniformly in the carbon matrix (Figure 3e). High magnification TEM image revealed the cobalt nanoparticles with around 10 nm embedded in nanoporous carbon (Figure 3f). In addition, the Co species migrated to form large Co nanoparticles during carbonization,

resulting in some large cavities with a diameter of several nanometres. By comparing the TEM results of Co-Zn-ZIF/GO-800 with Zn-ZIF/GO-800, the carbon nanosheets were more severely agglomerated. This may be caused by the cobalt species acting as a catalyst and converting amorphous carbon to the graphitized one.

XRD patterns of Zn-ZIF/GO-800 and Co-Zn-ZIF/GO-800 revealed a typical crystalline structure similar to ZIF-8, implying the nanoparticles deposited on GO showed an ordered microporous structure (Figure S8, Supporting Information). The addition of GO in the solution of ZIF clusters did not affect the formation of ordered microporous structure of ZIF. The peaks of GO were not observed owing to its lower intensity comparing with that of ZIF. After carbonization, the resultant Zn-ZIF/GO-800 material showed a carbon framework with partial graphitization. No peaks related to Zn crystals were seen, indicating that the zinc particles were fully removed by acid etching process, also confirmed by TEM results. By comparison, Co-Zn-ZIF/GO-800 revealed new peaks which can are related to the cobalt and Co_2N phase. The cobalt and Co_2N nanoparticles may be wrapped by the graphitic carbon tightly, and are retained in carbon matrix after acid leaching. Raman spectrum of both Zn-ZIF/GO-800 and Co-Zn-ZIF/GO-800 revealed D band (≈1350 cm^{-1}) and G band (≈1590 cm^{-1}), corresponding to the disorder and crystallinity of sp^2 hybrid carbon atoms, respectively (Figure S9, Supporting Information). Their I_D/I_G value (1.0) was greater than that of the graphene-based carbon materials GO-800 (0.93) prepared via carbonization of GO at 800 °C in Ar (Table S1, Supporting Information), indicating a lower degree of graphitization and high content of N atoms doped in the carbon lattice due to the coating of ZIF-derived carbon on graphene layer. In addition, after coating of ZIF-derived carbon materials on graphene, the 2D band of GO-800 disappeared, further proving the amorphous carbon was successfully coated on the graphene layer.

The specific surface area of the obtained carbon materials were measured using nitrogen sorption technique (**Figure 4**a). The Brunauer–Emmett–Teller (BET) surface area of Zn-ZIF/GO-800 was as high as 1170 $m^2\ g^{-1}$. By comparison, the carbon materials derived from the ZIF/GO-MIX-800 showed a lower specific surface area (823 $m^2\ g^{-1}$), indicating the uniformly distributions of ZIF nanoparticles can efficiently prevent the agglomeration of the GO layer. After incorporation of cobalt species, the specific surface area (373 $m^2\ g^{-1}$) decreased dramatically as the severe agglomeration of graphene during carbonization process, consistent with their appearance in the TEM results.

Note that pyridinic nitrogen and graphitic nitrogen are generally considered as the active sites for ORR, and pyridinic nitrogen and pyrrolic nitrogen can coordinate with Co to form Co-N_x moieties, which are more active than sole N-doped carbon for ORR.[18] X-ray photoelectron spectroscopy (XPS)

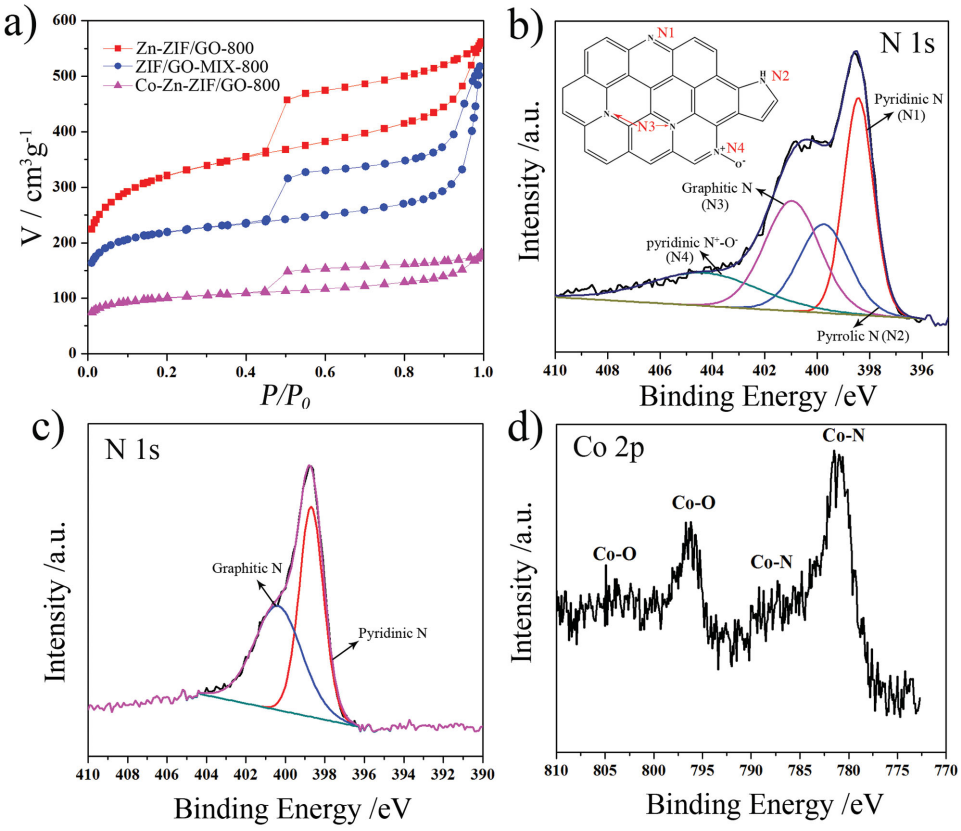

Figure 4. a) N_2 sorption isotherms of Zn-ZIF/GO-800, ZIF/GO-MIX-800, and Co-Zn-ZIF/GO-800; b,c) High-resolution N 1s spectra for Zn-ZIF/GO-800 and Co-Zn-ZIF/GO-800; d) High-resolution Co 2p spectra for Co-Zn-ZIF/GO-800. Inset in (b) are four different configurations for nitrogen atoms in the N-doped carbon materials (N1:Pyridinic N; N2:Pyrrolic N; N3:Graphitic N; N4:Pyridinic N^+–O^-).

analysis was used to investigate the chemical state of the nitrogen on the surface of carbon materials. The high resolution N 1s spectra for Zn-ZIF/GO-800 were fitted with four peaks at about 398.4, 399.7, 401.0, and 404.3 eV, corresponding to pyridinic nitrogen, pyrrolic nitrogen, graphitic nitrogen, and pyridinic N^+–O^-, respectively (Figure 4b). Their relative contents were 31.2%, 21.5%, 29.5%, and 17.8%, respectively. By comparison, the relative contents of N atoms in carbon lattice for ZIF/GO-MIX-800 were 40.1%, 18.2%, 24.0%, and 17.7% for pyridinic nitrogen, pyrrolic nitrogen, graphitic nitrogen, and pyridinic N^+–O^-, respectively (Figure S10, Supporting Information). Zn-ZIF/GO-800 and ZIF/GO-MIX-800 showed similar N atoms bonding configurations due to their same compositions and heat treatment conditions. The high resolution N 1s spectra for Co-Zn-ZIF/GO-800 were fitted with two peaks at 398.7 and 400.4 eV, corresponding to pyridinic nitrogen and graphitic nitrogen (Figure 4c). Their relative contents were 50.9 and 49.1%, respectively. The high content of pyridinic N^+–O^- found in Zn-ZIF/GO-800 and ZIF/GO-MIX-800 (≈18%) were not detected after introducing small amount of Co species in the carbon matrix, indicating that the Co species accelerate N incorporation into the carbon-ring, resulting in an ultrahigh content of graphitic nitrogen. In the Co 2p spectra for Co-Zn-ZIF/GO-800, the peak at about 780 and 786 eV assigned to Co–N species, while the peaks at 796.5 and 804.6 eV originate from Co–O species (Figure 4d). Both Co–N and Co–O species can enhance ORR catalytic activity in alkaline conditions, while Co–N sites play a key role in ORR performance in acidic conditions.

Due to the uniform nanoporous carbon/graphene/nanoporous carbon sandwich-like structure, high specific surface area and nitrogen-doping carbon framework, these materials were used as the nonprecious metal catalysts for oxygen reduction reaction, which is the important cathodic reaction of fuel cell and metal-air batteries. The concept of the designed materials for ORR was shown in **Figure 5**a. Graphene acts as a conductive layer to accelerate the electron transfer in the carbon matrix and readily reach to the active sites smoothly. Nanoporous carbon derived from ZIF acts as a catalytic layer, where the active sites (i.e., N-doping carbon, Co-N_x-C) were located in the nanoporous carbon. Due to its high specific surface area and nanoporous structure, large numbers of active sites are easily accessible by the reactants (i.e., O_2 and H_2O). In addition, the nanosheet structure also facilitates the fast transport of reactants to reach the active sites and removal of corresponding products (i.e., OH^-) from active sites due to the short transport pathway.

The ORR performance of the nanoporous carbon/graphene nanosheets was evaluated using a rotating disk electrode (RDE) technique. Cyclic voltammetry (CV) curves revealed a clearly

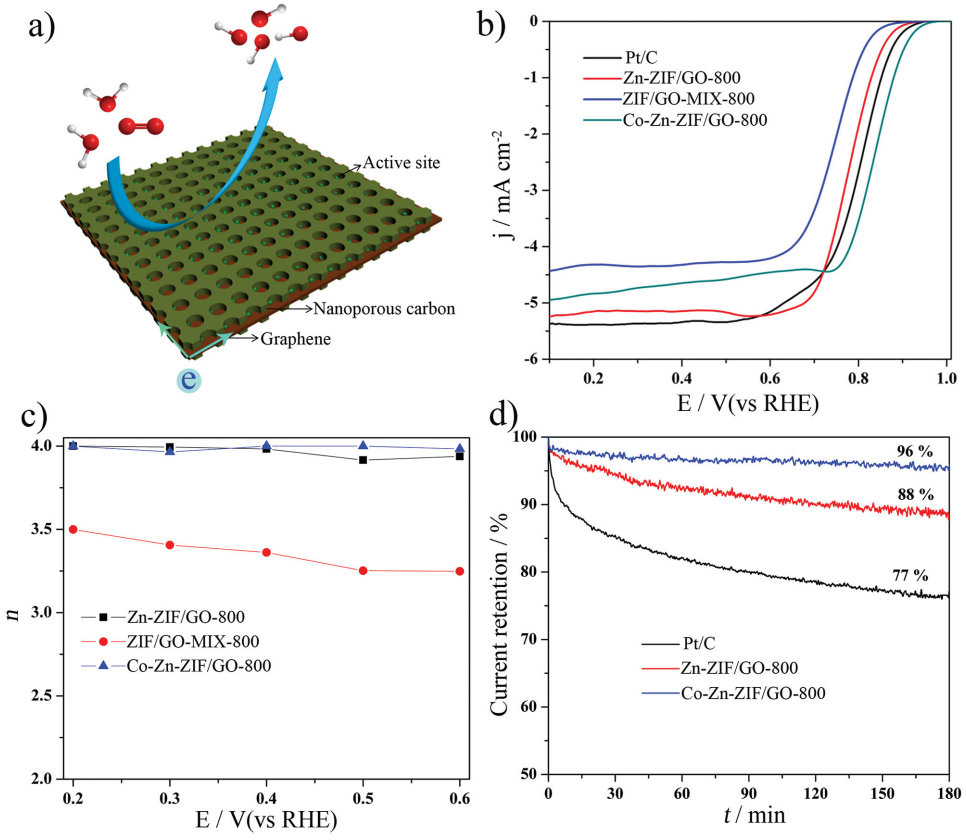

Figure 5. a) Schematic oxygen reduction process conducted on the nanoporous carbon/graphene sheets in alkaline conditions; b) LSV curves of commercial Pt/C, Zn-ZIF/GO-800, ZIF/GO-MIX-800, and Co-Zn-ZIF/GO-800 at 1600 rpm in O_2 saturated 0.1 M KOH solution; c) Electron transfer numbers of different catalysts from 0.2 to 0.6 V; d) Current–time chronoamperometric response of Pt/C, Zn-ZIF/GO-800, and Co-Zn-ZIF/GO-800 at 0.78 V with a rotating speed of 1600 rpm in O_2-saturated 0.1 M KOH solution.

oxygen reduction peaks for all the carbon materials (Pt/C, Zn-ZIF/GO-800, ZIF/GO-MIX-800, and Co-Zn-ZIF/GO-800) in O_2-saturated 0.1 M KOH solution comparing with that in N_2-saturated solution, implying an oxygen reduction activity (Figure S11, Supporting Information). The oxygen reduction peaks of Pt/C, Zn-ZIF/GO-800, ZIF/GO-MIX-800, and Co-Zn-ZIF/GO-800 were at 0.82, 0.74, 0.72, 0.82 V (vs RHE), respectively. Note that Zn-ZIF/GO-800 and ZIF/GO-MIX-800 were prepared using the same kind of precursor (ZIF-8 and GO) and carbonization condition. Their nitrogen atom bonding configurations were similar according to the XPS results. Zn-ZIF/GO-800 showed a more positive potential than ZIF/GO-MIX-800, indicating the uniform structure of ZIF/GO composites plays an important role in enhancing catalytic activity. Due to their regular structure, the agglomeration of graphene was effectively retarded, resulting in a high surface area and high density of active sites. After introduction of cobalt species in the carbon nanosheets, Co-Zn-ZIF/GO-800 showed a more positive potential (0.82 V), the same as the commercial Pt/C.

The linear scan voltammogram (LSV) curves revealed the same trend with the result of CV. The onset potential of Pt/C, Zn-ZIF/GO-800, ZIF/GO-MIX-800, and Co-Zn-ZIF/GO-800 were at 0.94, 0.92, 0.89, and 0.96 V (vs RHE), respectively (Figure 5b). Co-Zn-ZIF/GO-800 revealed even higher onset potential than commercial Pt/C, implying its high catalytic activity. The limiting currents at 0.60 V were 5.1, 5.2, 4.2, and 4.4 mA cm^{-2} for Pt/C, Zn-ZIF/GO-800, ZIF/GO-MIX-800, and Co-Zn-ZIF/GO-800, respectively. Zn-ZIF/GO-800 showed largest limiting current due to its high specific surface area. For Co-Zn-ZIF/GO-800 catalysts, the limiting current was a little lower than Pt/C and Zn-ZIF/GO-800 due to their low specific surface area, which may hinder fast mass transport and exchange at more negative potential.

The electron transfer number per oxygen molecule (n) for ORR was calculated from the LSV curves at different rotating speeds (400–2500 rpm) using Koutechy–Levich (K-L) equation. The K-L plots of Zn-ZIF/GO-800 within the potential range from 0.20 to 0.60 V exhibited good linearity with a similar slop (Figure S12, Supporting Information). The electron transfer number was determined to be about 4.0, indicating a four-electron pathway for ORR (Figure 4c). Using the same method, the electron transfer numbers of ZIF/GO-MIX-800 and Co-Zn-ZIF/GO-800 were 3.2–3.5 and ≈4.0, respectively. Zn-ZIF/GO-800 and Co-Zn-ZIF/GO-800 revealed a higher electron transfer number than ZIF/GO-MIX-800, indicating a low yield of intermediates (i.e., H_2O_2), which were produced via two-electron pathway.

The long-term stability of Zn-ZIF/GO-800, Co-Zn-ZIF/GO-800, and Pt/C for ORR was assessed and compared by chronoamperometric measurement at 0.78 V (vs RHE) in an O_2-saturated 0.1 M KOH solution. After 180 min of continuous operation, the commercial Pt/C showed a decrease of current by 23% (Figure 5d). By comparison, Zn-ZIF/GO-800 and Co-Zn-ZIF/GO-800 revealed a decrease of current by 12% and 4%, respectively. Such a high stability may be attributed to their unique nanosheet structure. The nanoporous carbon sheet with a rigid matrix facilitated the transport of reactant, intermediates and products, with the graphene layer maintaining a continuous electron-transport pathway for ORR. Unlike the Pt/C materials, the Pt nanoparticles were easily aggregated to lose their active surface. This result also revealed Co species can further enhance the stability of catalyst by increasing the degree of graphitization of nanoporous carbon.

Co-Zn-ZIF/GO-800 was also used as an ORR catalyst in acidic media (0.1 M $HClO_4$) due to its high catalytic performance and long-term stability in alkaline conditions. As shown in Figure S13, Supporting Information, CV curves of Co-Zn-ZIF/GO-800 showed an obvious oxygen reduction peak at 0.67 V, which was 110 mV negative to that of Pt/C (0.78 V). LSV curves of Co-Zn-ZIF/GO-800 and Pt/C revealed their onset potentials are 0.85 and 0.93 V, respectively (**Figure 6**a). The limiting current of Co-Zn-ZIF/GO-800 and Pt/C at 0.40 V were 4.2 and 5.7 mA cm^2, respectively. The onset potential and limiting current density of Co-Zn-ZIF/GO-800 were 70 mV and 1.5 mA cm^{-2} lower than Pt/C. The LSV curves at different rotation speeds (400–2500 rpm) revealed the same onset potential (Figure 6b). The K-L plots derived from Figure 6b showed a good linearity and parallelism over the entire potential range (0.2–0.5 V), indicating that their electron transfer number for ORR is similar. The electron transfer numbers for Co-Zn-ZIF/GO-800 is around 4.0, implying a 4e process in acid media (Figure 6c). The ORR performance of Zn-ZIF/GO-800 and Co-Zn-ZIF/GO-800 in both alkaline and acidic conditions is among the best of nonprecious metal catalyst reported so far (Tables S2 and S3, Supporting Information). Co-Zn-ZIF/GO-800 revealed a much higher stability than Pt/C from the results of chronoamperometric measurement operated at 0.72 V (Figure 6d). After 180 min of reaction, the current of Co-Zn-ZIF/GO-800 only showed a loss of 16% while that of Pt/C revealed a loss of 93%. In addition, Co-Zn-ZIF/GO-800 showed a higher resistance to the methanol cross-over effect than Pt/C, implying good catalytic selectivity (Figure S14, Supporting Information). The good methanol tolerance is of particular important in practical applications for direct methanol fuel cell.

3. Conclusion

In conclusion, we have demonstrated that a simple ZIF nanocrystals layer produced on graphene oxide were able to cause protected carbonization to prepare N-doped nanoporous carbon/graphene/N-doped nanoporous carbon nano-sandwiches. The uniform ZIF/GO/ZIF sandwich-like structure with around 20 nm in size fully covering both sides of GO were firstly synthesized. The synthesis mechanism involved homogenous nucleation of ZIF, followed by the deposition of ZIF on GO and a confined growth process. The continuous ZIF layer was able to not only effectively prevent the agglomeration of graphene during high-temperature treatment, but also was converted to the N-doped nanoporous carbon layer with high density of active sites for electrocatalysis. The resultant carbon nanosheets revealed a high specific surface area (1170 cm^2 g^{-1}), nanoporous structure and good electrical conductivity, all of which assist fast mass transport and electron transfer required by ORR. As a result, the N-doped nanoporous carbon/graphene nanosheets showed a high onset potential (i.e., 0.92 V) and limiting current density (i.e., 5.2 mA cm^{-2} at 0.60 V vs RHE) when used as the electrocatalysts for the oxygen reduction in 0.1 M

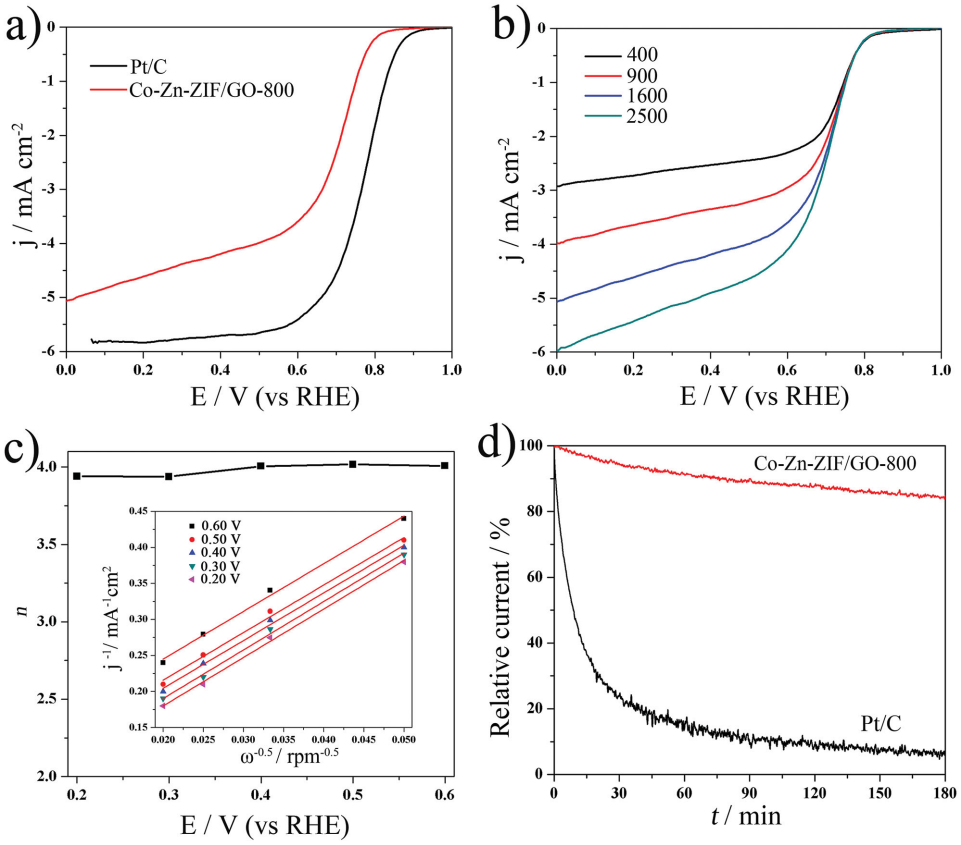

Figure 6. a) LSV curves of commercial Pt/C and Co-Zn-ZIF/GO-800 at 1600 rpm in O_2 saturated 0.1 M $HClO_4$ solution; b) LSV curves of Co-Zn-ZIF/GO-800 at different rotation speeds (400–2500 rpm); c) Electron transfer numbers for Co-Zn-ZIF/GO-800 from 0.2 to 0.6 V; inset in (c) is K-L plots at different potentials; d) Current–time chronoamperometric response of Pt/C and Co-Zn-ZIF/GO-800 at 0.72 V with a rotating speed of 1600 rpm in O_2-saturated 0.1 M $HClO_4$ solution.

KOH. By introduction of cobalt species in the carbon materials, the Co-N_x/carbon materials revealed a higher onset potential (0.96 V) than both commercial Pt/C (0.94 V) and N-doped nanoporous carbon/graphene nanosheets. Furthermore, nanoporous Co-N_x/carbon nanosheets showed good electrocatalytic activity in acidic media, with an onset potential (0.85 V) comparable with commercial Pt/C (0.93 V). Most importantly, the nanoporous Co-N_x/carbon nanosheets revealed a higher long-term stability and better methanol tolerance than Pt/C materials in acidic media. This work represents a new ZIF layer protected carbonization method to construct functional nanoporous carbon/graphene nanosheets with high specific surface area. Additionally, such N-doped carbon/graphene nanosheets can also be used for other potential applications such as CO_2 adsorption, supercapacitors, batteries, and water splitting.

4. Experimental Section

Synthesis of Zn-ZIF/GO: Graphene oxide (GO) was prepared via modified Hummer method.[19] 0.366 g of $Zn(NO_3)_2{\cdot}6H_2O$ and 0.811 g of 2-methylimidazole (mim) were dissolved in 12 and 20 mL of methanol, respectively. Then, $Zn(NO_3)_2$ solution (12 mL) was added into the 2-methylimidazole solution to obtain a clear solution. 8 mL of GO solution (1 mg mL^{-1}, in water/methanol, 1:4, v/v) was immediately added to the above mixed solution. After stirring for 3 h, the gray precipitation was collected by centrifugation (8000 rpm for 3 min) and washing with methanol at least three times. After drying at 50 °C for 12 h, ZIF/GO was prepared, which was denoted as Zn-ZIF/GO.

Synthesis of Co-Zn-ZIF/GO: the synthesis procedure is the same as that of Zn-ZIF/GO except replacement of 10 wt% of $Zn(NO_3)_2{\cdot}6H_2O$ with $Co(NO_3)_2{\cdot}6H_2O$ (9:1) as metal ion precursor.

Synthesis of ZIF/GO-MIX: By comparison, GO solution was first added into the $Zn(NO_3)_2$ solution. The mim solution was then added into the mixture. After stirring for 3 h, the obtained samples were denoted as ZIF/GO-MIX. The ratio of GO:Zn:mim keeps constant with that of Zn-ZIF/GO.

Synthesis of ZIF/GO-Derived Carbon Materials: Zn-ZIF/GO, Co-Zn-ZIF/GO, and ZIF/GO-MIX were calcined at 800 °C for 3 h in Ar atmosphere. Then the carbon composites were immersed in 2 M HCl aqueous solution for 12 h and collected by centrifugation and washing with water. After drying at 80 °C for 24 h, Zn-ZIF/GO-800, Co-Zn-ZIF/GO-800, and ZIF/GO-MIX-800 were obtained.

Characterization: SEM images were taken with a field-emission scanning electron microscope (FEI Nova NanoSEM 450) operating at 5 kV. TEM images were taken by a FEI Tecnai G2 F20 and FEI Tecnai G2 T20 operated at an accelerating voltage of 200 kV. The samples were first dispersed in ethanol. A drop of the dispersion was supported on a copper grid with holey carbon films and then dried, prior to TEM characterization. Nitrogen adsorption/desorption isotherms were measured at −196 °C with a Micromeritics Tristar Analyzer. Before measurements, the samples were degassed in a vacuum at 180 °C for at least 12 h. The BET method was utilized to calculate the specific surface area by using the adsorption data at p/p_0 range of 0.05–0.25. XPS experiments were carried out on a Kratos AXIS Ultra DLD system with

Al Kα radiation as X-ray source for radiation. Powder X-ray diffraction (PXRD) patterns were recorded in the 2θ range of 5°–80° at room temperature using a Miniflex 600 diffractometer (Rigaku, Japan) in a transmission geometry using Cu Kα radiation (15 mA and 40 kV) at a scan rate of 2° min^{-1} and a step size of 0.02°. The Raman spectra were recorded on a WITEC Alpha 300 confocal micro-Raman system equipped with a 532 nm laser source and 100× objective lens. The carbon powders were sandwiched with two glass slides before the test.

Electrochemical Measurements: CV and LSV voltammetry were performed by using a μAutolab electrochemical analyzer in a conventional three-electrode electrochemical cell. A Pt wire auxiliary electrode, a saturated Ag/AgCl (saturated with 3 M KCl) reference electrode, and rotating disk working electrode were used. For the ORR, 4 mg of catalysts (or commercial Pt/C, 20 wt%, from Sigma-Aldrich) were dispersed in 1 mL of ethanol (containing 0.03 mL of 5.0 wt% Nafion) solution under ultrasonic agitation to form an electrocatalyst ink. Then 10 (15 for acidic conditions) μL of the electrocatalyst ink (5 μL for Pt/C) was dropped on the surface of the precleaned rotating disk electrode (5 mm diameter, 0.196 cm^2) and dried at room temperature. The non-precious metal catalyst loading amounts are 0.2 mg cm^{-2} in 0.1 M KOH and 0.3 mg cm^{-2} in 0.1 M $HClO_4$. A 0.1 M KOH (or 0.1 M $HClO_4$) solution was used as the electrolyte for all the CV and RDE studies. Argon and O_2 were used to achieve oxygen-free and oxygen-rich environments. The electrolyte was saturated with Ar (or O_2) before test. The CV curves were recorded at a scan rate of 50 mV s^{-1}; the RDE curves were recorded at a scan rate of 10 mV s^{-1}. A flow of O_2 was maintained over the electrolyte during the CV and LSV test to ensure O_2 saturation. The numbers of electrons transferred (n) during ORR was calculated by Koutecky–Levich equation, at various electrode potentials:

$$\frac{1}{J} = \frac{1}{J_L} + \frac{1}{J_K} = \frac{1}{B\omega^{0.5}} + \frac{1}{J_K}$$

$$B = 0.62nFC_0D_0^{2/3}\nu^{-1/6}$$

where J is the measured current density, J_K and J_L are the kinetic and diffusion-limiting current densities, ω is the angular velocity, n is transferred electron number, F is the Faraday constant (96 485 C mol^{-1}), C_0 is the bulk concentration of O_2 (1.2×10^{-6} mol cm^{-3} for 0.1 M KOH, 1.26×10^{-6} mol cm^{-3} for 0.1 M $HClO_4$), D_0 is the diffusion coefficient of O_2 (1.9×10^{-5} cm^2 s^{-1} in 0.1 M KOH, 1.93×10^{-5} cm^2 s^{-1} in 0.1 M $HClO_4$), and ν is the kinematic viscosity of the electrolyte (0.01 cm^2 s^{-1} in 0.1 M KOH, 0.01009 cm^2 s^{-1} in 0.1 M $HClO_4$).

Supporting Information

Supporting Information is available from the Wiley Online Library or from the author.

Acknowledgements

This work was supported by the Australian Research Council (Discovery Project No. DP150100765). The authors thank the staff of Monash Centre for Electron Microscopy for their technical assistance in SEM and TEM.

Received: June 7, 2015
Revised: July 21, 2015
Published online: August 13, 2015

[1] a) A. Stein, Z. Y. Wang, M. A. Fierke, *Adv. Mater.* **2009**, *21*, 265; b) Y. Zhai, Y. Dou, D. Zhao, P. F. Fulvio, R. T. Mayes, S. Dai, *Adv. Mater.* **2011**, *23*, 4828; c) Y. Mao, H. Duan, B. Xu, L. Zhang, Y. Hu, C. Zhao, Z. Wang, L. Chen, Y. Yang, *Energy Environ. Sci* **2012**, *5*, 7950; d) L. Dai, L. Qu, H. Choi, J. Baek, *Chem. Rev.* **2015**, *115*, 4823; e) W. Xia, R. Zou, Q. Xu, *Energy Environ. Sci.* **2015**, *8*, 1837; f) S. L. Candelaria, Y. Y. Shao, W. Zhou, X. L. Li, J. Xiao, J. G. Zhang, Y. Wang, J. Liu, J. H. Li, G. Z. Cao, *Nano Energy* **2012**, *1*, 195; g) Y. Zheng, Y. Jiao, M. Jaroniec, Y. Jin, S. Z. Qiao, *Small* **2012**, *8*, 3550; h) B. Sun, X. Huang, S. Chen, P. Munroe, G. Wang, *Nano Lett.* **2014**, *14*, 3145.

[2] a) Y. Zheng, J. Liu, J. Liang, M. Jaroniec, S. Z. Qiao, *Energy Environ. Sci.* **2012**, *5*, 6717; b) D.-W. Wang, D. Su, *Energy Environ. Sci.* **2014**, *7*, 576; c) N. Daems, X. Sheng, I. F. J. Vankelecom, P. P. Pescarmona, *J. Mate. Chem. A* **2014**, *2*, 4085; d) J. Song, T. Xu, M. L. Gordin, P. Zhu, D. Lv, Y.-B. Jiang, Y. Chen, Y. Duan, D. Wang, *Adv. Funct. Mater.* **2014**, *24*, 1243; e) K. Gong, F. Du, Z. Xia, M. Durstock, L. Dai, *Science* **2009**, *323*, 760; f) R. Liu, D. Wu, X. Feng, K. Müllen, *Angew. Chem. Int. Ed.* **2010**, *49*, 2565; g) J. Wei, D. Zhou, Z. Sun, Y. Deng, Y. Xia, D. Zhao, *Adv. Funct. Mater.* **2013**, *23*, 2322.

[3] a) B. Liu, H. Shioyama, T. Akita, Q. Xu, *J. Am. Chem. Soc.* **2008**, *130*, 5390; b) B. Liu, H. Shioyama, H. Jiang, X. Zhang, Q. Xu, *Carbon* **2010**, *48*, 456; c) S. J. Yang, T. Kim, J. H. Im, Y. S. Kim, K. Lee, H. Jung, C. R. Park, *Chem. Mater.* **2012**, *24*, 464; d) W. Chaikittisilp, K. Ariga, Y. Yamauchi, *J. Mater. Chem. A* **2013**, *1*, 14; e) T. Palaniselvam, B. P. Biswal, R. Banerjee, S. Kurungot, *Chem. Eur. J.* **2013**, *19*, 9335; f) X. Wang, J. Zhou, H. Fu, W. Li, X. Fan, G. Xin, J. Zheng, X. Li, *J. Mater. Chem. A* **2014**, *2*, 14064; g) P. Zhang, F. Sun, Z. Xiang, Z. Shen, J. Yun, D. Cao, *Energy Environ. Sci.* **2014**, *7*, 442; h) D. Zhao, J.-L. Shui, L. R. Grabstanowicz, C. Chen, S. M. Commet, T. Xu, J. Lu, D.-J. Liu, *Adv. Mater.* **2014**, *26*, 1093; i) F. Zheng, Y. Yang, Q. Chen, *Nat. Commun.* **2014**, *5*, 5261; j) F. Zou, X. Hu, Z. Li, L. Qie, C. Hu, R. Zeng, Y. Jiang, Y. Huang, *Adv. Mater.* **2014**, *26*, 6622; k) D. Y. Chung, K. J. Lee, S.-H. Yu, M. Kim, S. Y. Lee, O.-H. Kim, H.-J. Park, Y.-E. Sung, *Adv. Energy Mater.* **2015**, *5*, 1401309; l) Y. Hou, Z. Wen, S. Cui, S. Ci, S. Mao, J. Chen, *Adv. Funct. Mater.* **2015**, *25*, 872.

[4] W. Chaikittisilp, N. L. Torad, C. Li, M. Imura, N. Suzuki, S. Ishihara, K. Ariga, Y. Yamauchi, *Chem. Eur. J.* **2014**, *20*, 4217.

[5] a) W. Xia, J. Zhu, W. Guo, L. An, D. Xia, R. Zou, *J. Mater. Chem. A* **2014**, *2*, 11606; b) L. Zhang, Z. Su, F. Jiang, L. Yang, J. Qian, Y. Zhou, W. Li, M. Hong, *Nanoscale* **2014**, *6*, 6590.

[6] H. Zhong, J. Wang, Y. Zhang, W. Xu, W. Xing, D. Xu, Y. Zhang, X. Zhang, *Angew. Chem. Int. Ed.* **2014**, *53*, 14235.

[7] E. Antolini, *Appl. Catal. B: Environ.* **2009**, *88*, 1.

[8] a) A. Fasolino, J. H. Los, M. I. Katsnelson, *Nat. Mater.* **2007**, *6*, 858; b) A. K. Geim, K. S. Novoselov, *Nat. Mater.* **2007**, *6*, 183; c) F. Bonaccorso, L. Colombo, G. Yu, M. Stoller, V. Tozzini, A. C. Ferrari, R. S. Ruoff, V. Pellegrini, *Science* **2015**, *347*, 1246501.

[9] Z. Lei, N. Christov, X. S. Zhao, *Energy Environ. Sci.* **2011**, *4*, 1866.

[10] a) Z.-S. Wu, Y. Sun, Y.-Z. Tan, S. Yang, X. Feng, K. Müllen, *J. Am. Chem. Soc.* **2012**, *134*, 19532; b) Z. Fan, J. Yan, L. Zhi, Q. Zhang, T. Wei, J. Feng, M. Zhang, W. Qian, F. Wei, *Adv. Mater.* **2010**, *22*, 3723; c) H. Sun, Z. Xu, C. Gao, *Adv. Mater.* **2013**, *25*, 2554; d) S. Yang, X. Feng, X. Wang, K. Müllen, *Angew. Chem. Int. Ed.* **2011**, *50*, 5339; e) S. Yang, L. Zhi, K. Tang, X. Feng, J. Maier, K. Müllen, *Adv. Funct. Mater.* **2012**, *22*, 3634; f) Z.-S. Wu, S. Yang, Y. Sun, K. Parvez, X. Feng, K. Müllen, *J. Am. Chem. Soc.* **2012**, *134*, 9082; g) B. G. Choi, M. Yang, W. H. Hong, J. W. Choi, Y. S. Huh, *Acs Nano* **2012**, *6*, 4020.

[11] S. Yang, X. Feng, L. Wang, K. Tang, J. Maier, K. Müllen, *Angew. Chem. Int. Ed.* **2010**, *49*, 4795.

[12] H. B. Wu, B. Y. Xia, L. Yu, X.-Y. Yu, X. W. D. Lou, *Nat. Commun.* **2015**, *6*, 6512.

[13] a) Y. Zheng, Y. Jiao, J. Chen, J. Liu, J. Liang, A. Du, W. Zhang, Z. Zhu, S. C. Smith, M. Jaroniec, G. Q. Lu, S. Z. Qiao, *J. Am. Chem. Soc.* **2011**, *133*, 20116; b) Y. Sun, C. Li, G. Shi, *J. Mater. Chem.* **2012**, *22*, 12810; c) Y. Fang, Y. Lv, R. Che, H. Wu, X. Zhang, D. Gu, G. Zheng, D. Zhao, *J. Am. Chem. Soc.* **2013**, *135*, 1524; d) W. Wei, H. Liang, K. Parvez, X. Zhuang, X. Feng, K. Müllen, *Angew. Chem.*

Int. Ed. **2014**, *53*, 1570; e) B. Y. Xia, Y. Yan, X. Wang, X. W. Lou, *Mater. Horiz.* **2014**, *1*, 379; f) Y. Ito, H. J. Qiu, T. Fujita, Y. Tanabe, K. Tanigaki, M. Chen, *Adv. Mater.* **2014**, *26*, 4145.

[14] a) R. Kumar, K. Jayaramulu, T. K. Maji, C. N. R. Rao, *Chem. Commun.* **2013**, *49*, 4947; b) X. Cao, B. Zheng, X. Rui, W. Shi, Q. Yan, H. Zhang, *Angew. Chem. Int. Ed.* **2014**, *53*, 1404; c) X. Huang, B. Zheng, Z. Liu, C. Tan, J. Liu, B. Chen, H. Li, J. Chen, X. Zhang, Z. Fan, W. Zhang, Z. Guo, F. Huo, Y. Yang, L.-H. Xie, W. Huang, H. Zhang, *ACS Nano* **2014**, *8*, 8695; d) X. Qiu, X. Wang, Y. Li, *Chem. Commun.* **2015**, *51*, 3874; e) J. Wei, Y. X. Hu, Z. X. Wu, Y. Liang, S. Leong, B. Kong, X. Y. Zhang, D. Y. Zhao, G. P. Simon, H. T. Wang, *J. Mater. Chem. A* **2015**, DOI: 10.1039/C5TA04330A.

[15] I. H. Lim, W. Schrader, F. Schüth, *Chem. Mater.* **2015**, *27*, 3088.

[16] C.-N. Yeh, K. Raidongia, J. Shao, Q.-H. Yang, J. Huang, *Nat. Chem.* **2015**, *7*, 166.

[17] a) C. W. B. Bezerra, L. Zhang, K. Lee, H. Liu, A. L. B. Marques, E. P. Marques, H. Wang, J. Zhang, *Electrochim. Acta* **2008**, *53*, 4937; b) R. Jasinski, *Nature* **1964**, *201*, 1212.

[18] G. Wu, P. Zelenay, *Acc. Chem. Res.* **2013**, *46*, 1878.

[19] W. S. Hummers Jr., R. E. Offeman, *J. Am. Chem. Soc.* **1958**, *80*, 1339.